

Enhancement of Terrestrial Diffuse X-ray Emission Associated With Coronal Mass Ejection and Geomagnetic Storm

Yuichiro EZOE¹, Yoshizumi MIYOSHI², Hiroshi YOSHITAKE³, Kazuhisa MITSUDA³,
Naoki TERADA⁴, Shihoko OISHI¹, and Takaya OHASHI¹

¹ *Tokyo Metropolitan University, 1-1, Minami-Osawa, Hachioji, Tokyo, 192-0397, JAPAN*

² *Nagoya University, Furo-cho, Chikusa-ku, Nagoya 464-8601, JAPAN*

³ *The Institute of Space and Astronautical Science (ISAS), Japan Aerospace and eXpoloration Agency (JAXA), 3-1-1 Yoshinodai, Sagamihara, Kanagawa 229-8510, JAPAN*

⁴ *Tohoku University, 6-3, Aoba, Aramaki-za, Sendai, Miyagi 980-8578, JAPAN*

ezoe@phys.metro-u.ac.jp

(Received ; accepted)

Abstract

We present an analysis of a Suzaku observation taken during the geomagnetic storm of 2005 August 23-24. We found time variation of diffuse soft X-ray emission when a coronal mass ejection hit Earth and caused a geomagnetic storm. The diffuse emission consists of fluorescent scattering of solar X-rays and exospheric solar wind charge exchange. The former is characterized by a neutral oxygen emission line due to strong heating of the upper atmosphere during the storm time, while the latter is dominated by a sum of C V, C VI, N VI, N VII, O VII, and O VIII emission lines due to the enhanced solar wind flux in the vicinity of the exosphere. Using the solar wind data taken with the ACE and WIND satellites, a time correlation between the solar wind and the strong O VII line flux were investigated. We estimated necessary column densities for the solar X-ray scattering and exospheric SWCX. From these results, we argue that a part of the solar wind ions enter inside the magnetosphere and cause the SWCX reaction.

Key words: X-ray: diffuse background — Sun: solar wind — Sun: solar-terrestrial relations — Earth

1. Introduction

A coronal mass ejection (CME) is a large burst of coronal magnetic fields and plasma with a typical mass of 10^{15-16} g and speeds of 250-1000 km s⁻¹ into interplanetary space

(Gosling 1997; Hudson et al. 2010). CMEs are often associated with solar flares and prominence eruptions. The occurrence of CMEs depends on the phase of the solar cycle. The ejected CMEs that move toward Earth drive interplanetary shocks and trigger geomagnetic storms (e.g., Gonzalez et al. 1994; Miyoshi & Kataoka 2005). Such geomagnetic storms pose significant hazards to space operations. Enhancements of trapped particles of the radiation belts increase spacecraft charging and solar energetic protons cause single event upset (Pilipenko et al. 2006). Atmospheric heating by the charged particles and solar ultraviolet/X-ray emission causes the Earth's upper atmosphere to expand, and leads to satellite drag (Doornbos et al. 2006).

For general users of X-ray astronomy satellites, signals associated with CMEs and geomagnetic storms may constitute additional sources of background when they observe astrophysical objects. Increased scattering of solar X-rays by the Earth's atmosphere is often seen in satellite data. This scattering is due to Thomson scattering of solar X-rays by electrons in the sunlit atmosphere and absorption of incident solar X-rays followed by the emission of characteristic K lines (Petrinec et al. 2000). Removal of time durations when the line of sight direction is near the sunlit atmosphere is effective in removing this emission.

Another major background is solar wind charge exchange (SWCX). This occurs when an ion in the solar wind interacts with a neutral atom. The ion strips an electron(s) from the atom, and then X-ray or ultraviolet photon(s) are released as the electron relaxes into the ground state. Short-term variations from SWCX in Earth's exosphere (Snowden et al. 2004; Wargelin et al. 2004; Fujimoto et al. 2007; Carter & Sembay 2008; Ezoe et al. 2010; Ezoe et al. 2011; Carter et al. 2011) or longer-term variations from SWCX in interplanetary space (Smith et al. 2005) and heliosphere (Cravens 2000; Koutroumpa et al. 2007; Koutroumpa et al. 2009), can produce diffuse X-ray emission below ~ 2 keV. To characterize the SWCX emission in an astrophysical data set, careful checks of an X-ray light curve and simultaneously observed solar wind data are indispensable.

The terrestrial diffuse X-ray emission, i.e., scattering of solar X-rays and exospheric SWCX, provides valuable information concerning the atmospheric expansion, the exospheric density, the constituents of the solar wind, and the transport processes of the plasma within the bow shock. Carter & Sembay (2008) systematically searched for the exospheric SWCX emission from data in the XMM-Newton Archive. Approximately 3.4 % of observations were affected by the exospheric SWCX (Carter et al. 2011). Most of the SWCX emission were seen when XMM-Newton observes through the sub-solar side of the magnetosheath. In some cases, the SWCX emission was seen when the line of sight direction did not intersect the high flux region. They reasoned that these cases probably originate from CMEs. They studied the most spectrally rich example of SWCX and argued that this event was associated with a CME recorded on 2001 October 21 (Carter, et al. 2010).

Thanks to a good energy response and the low instrument background of the X-ray CCDs (X-ray Imaging Spectrometer, XIS: Koyama et al. 2007), the fifth Japanese X-ray astronomical

satellite Suzaku (Mitsuda et al. 2007) is ideal for studying the terrestrial diffuse X-ray emission. Fujimoto et al. (2007) discovered an exospheric SWCX event in the direction of the north ecliptic pole. Their data indicated that a distance to the point where the geomagnetic field becomes open to space for the first time in the line of sight may be closely related to the short term SWCX variability. Ezoe et al. (2010) found another exospheric SWCX event toward the sub-solar side of the magnetosheath. They conducted a cross correlation analysis using the Suzaku OVII X-ray light curve and the ACE solar wind O^{7+} curve, and found a significant correlation between them. The necessary column density of neutral hydrogen atoms in the Earth’s exosphere to explain the observed X-ray flux exceeded that predicted by the exosphere model by a factor of 10. They reasoned that the discrepancy can be due to uncertainty of the model itself and/or solar wind distribution in the magnetosphere.

In this paper, we present evidence of a strong enhancement of the terrestrial diffuse X-ray emission associated with a strong geomagnetic storm recorded on 2005 August 24. The event under analysis occurred during the solar declining phase of solar cycle 23. We utilized the Dst index as an indicator of the geomagnetic storm. This is an index for the world wide magnetic storm level and constructed by averaging the horizontal component of the geomagnetic field from mid-latitude and equatorial magnetometer data. Negative Dst values caused by the storm time ring current indicate a magnetic storm is in progress. The Dst index is provided by the World Data Center for Geomagnetism, Kyoto, Japan¹. The storm studied in this paper is strongest with the Dst index of -216 nT that Suzaku has experienced as of 2011 April.

2. Observation

The Suzaku observation on 2005 August 23-24 was toward the PSR B1509–58 (RA = 228.484 deg, Dec = -59.136 deg, $l = 320.322$ deg, $b = -1.163$ deg). The Suzaku observation ID is 100009010. This field contains a bright X-ray pulsar, a pulsar wind nebula (PWN), and the hot nebula RCW 89. The Galactic column in the direction of this field as estimated using the HEASARC nH tool² is 1.4×10^{22} cm⁻². The average line of sight vector in the GSE and GSM coordinates are $(-0.0395, 0.7717, -0.6343)$ and $(-0.0395, 0.5811, -0.8124)$, respectively. In figure 1, we plot the line of sight during the observation. It is toward the south direction, while the past two Suzaku detections of exospheric SWCX events were toward the north ecliptic pole and magnetosheath. The observation starts from 2005 August 23 (the Day of Year, DOY, of 235 in 2005) 08:38 and ends August 24 (DOY of 236) 20:38.

The original aim of the observation was timing calibration using the pulsation period of the pulsar that has been published by Terada et al. (2008). For this purpose, in a part of the observation, the XIS was operated at timing mode, in addition to normal clocking

¹ <http://wdc.kugi.kyoto-u.ac.jp/dstdir/>

² <http://heasarc.gsfc.nasa.gov/cgi-bin/Tools/w3nh/w3nh.pl>

mode. Because the imaging capability is not available in the timing mode, we analyzed only the normal clocking mode data. The effective exposure time of the normal clocking mode data after standard data screening is 59 ks. The process version is 2.0.6.13. The HEASoft analysis package (version 6.4)³ was used to extract images, light curves, spectral products and instrumental response files.

We created XIS images in three representative energy bands from BI (back-illuminated, XIS1) and FI (front-illuminated, XIS0, 2, and 3) cameras as shown in figure 2. Two diffuse X-ray emission at the positions of the pulsar and PWN, and RCW 89 are observed. The pulsar and PWN emissions located in the south east becomes dominant in the hard X-ray band, while the north nebula RCW 89 is brighter in the soft band. Past higher resolution Chandra images showed similar tendencies (figure 6 in Gaensler et al. 2002). From these past observations, the pulsar and PWN are known to have a hard power law spectrum, while the spectrum of RCW 89 is dominated by a thermal plasma emission. To minimize contamination from these X-ray sources, we chose three corner regions for the following light curve and spectral analyses. Hereafter we call a sum of the three regions a terrestrial diffuse X-ray emission (TDX) region. A total area of the TDX region is 41.9 arcmin².

3. Light Curve

In figure 3, we plot X-ray light curves extracted from the TDX region in two energy bands that could potentially contain oxygen emission lines from scattering of solar X-rays and/or SWCX (0.5–0.7 keV) and for comparison a non-SWCX continuum at high energies (2.5–5 keV), similar to Carter & Sembay (2008). The 0.5–0.7 keV count rate shows a clear enhancement from DOY of 236.3 to 236.8. The average rate in the first half of the observation (pre-storm period in figure 3) and the second half covering (storm period) are 0.0057 ± 0.0008 and 0.013 ± 0.001 cts sec⁻¹, respectively. Errors are 2σ significance. In contrast, the 2.5–5 keV count rate shows less variability with the average rates in the pre-storm and storm periods of 0.054 ± 0.002 and 0.055 ± 0.002 cts sec⁻¹, although we see some rapid rises before data gaps (e.g., at DOY of 236.4) and a gradual change around DOY of 236.55.

Several data points both in 0.5–0.7 and 2.5–5 keV show the very rapid short term increases in the storm period. The scattering of solar X-rays is known to vary depending on the elevation angle (ELV) of the line of sight from Earth rim. Because Suzaku orbits around Earth once per ~ 90 min, a part of the observation suffers from Earth occultation. The periodic data gaps seen in figure 3 correspond to such occultations. The high count rate bins are seen just before the occultation when the ELV angle is relatively small ~ 5 deg. Thus, the observed short-term enhancements are most probably scattering of solar X-rays. A detailed spectral analysis will be done in §6.1.

³ <http://heasarc.gsfc.nasa.gov/docs/software/lheasoft/>

Using the same time axis, we plot the SYM-H index provided by the World Data Center for Geomagnetism, Kyoto, Japan⁴, and the solar proton flux as measured by WIND⁵. The SYM-H index is an indicator of the total energy content of the ring current almost similar to the hourly Dst index but with a high time resolution (1 min) (Wanliss & Showalter 2006). The SYM-H index exhibits three prototypical periods of the geomagnetic storm. The first period is a storm sudden commencement (SSC) at DOY of 236.26, corresponding to a sharp rise of the SYM-H index, when the CME-induced shock arrived at Earth. The second one is the storm main phase consisting of a dramatic decrease of the SYM-H index to a minimum value (-174 nT) when a ring current around Earth is built up due to high energy particle enhancements (e.g., Gonzalez et al. 1994; Miyoshi & Kataoka 2005). The final one is the storm recovery phase seen from DOY of 236.45 when the SYM-H index had a minimum value.

The solar wind proton data taken with WIND provides more information on the solar wind propagation toward Earth. The WIND satellite at this observation time was around the sunward L1 Lagrangian point, approximately 230 earth radii (R_E) from Earth. From the solar wind proton flux and solar wind dynamic pressure in figure 3, discontinuous rises can be seen at DOY of 236.23 that should be related to the CME-induced shock. Assuming the average proton speed during the observation of 530 km s^{-1} , an expected delay of the solar wind to move from the L1 point to Earth becomes 0.03 days. Therefore, an estimated arrival time of the shock at Earth considering the delay becomes DOY of 236.26 that coincides well with the SSC, i.e., the onset of the geomagnetic storm, seen in the ground-based SYM-H index.

Compared to the SYM-H index and solar wind, the enhancements of the X-ray light curves in 0.5–0.7 and 2.5–5.0 keV occurred after the SSC and the increase of the solar wind proton flux as well as the dynamic pressure. Therefore, the X-ray enhancements should be closely related to the increased solar wind near Earth. More specifically, the soft X-ray enhancement is indicative of the exospheric SWCX emission induced by the CME, while that in the hard X-ray band can be related to increased particle backgrounds.

To check whether this time variability is due to leaked photons from the bright X-ray sources, we created ratio maps between the storm and pre-storm periods as shown in figure 4. In 0.5–0.7 keV, the TDX region shows a factor of ~ 2 increase, while the bright X-ray sources are rather steady. In 2–5 keV, the entire field of view becomes steady. Therefore, the soft X-ray enhancements must be related to the geomagnetic storm and not due to changes in the leaked photons from the bright X-ray sources.

⁴ <http://wdc.kugi.kyoto-u.ac.jp/aeasy/index.html>

⁵ http://web.mit.edu/space/www/wind_data.html

4. Spectrum

We extracted the XIS spectra of the TDX region during the pre-storm and storm periods as shown in figure 5. Backgrounds are not subtracted. The XIS BI spectrum during the storm period (green) clearly shows an excess below ~ 1 keV compared to that in the pre-storm period (black). Signatures of the carbon (~ 0.3 keV), nitrogen (~ 0.4 keV) and oxygen (0.5–0.6 keV) emission lines are seen. There is also a spectrally smooth excess above ~ 2 keV. On the other hand, the FI spectrum during the storm period exhibits a clear excess only below 1 keV. Because the FI CCDs have a higher sensitivity above 1 keV than the BI, the hard X-ray excess seen in the BI spectrum will not arise from X-ray photons but particle backgrounds. Ionization particles such as soft protons can produce this spectrally smooth, flat, wide-band, whole field-of-view signal (e.g., Carter & Sembay 2008). These particles are funnelled by the telescope onto the CCD, and generate signals. The BI CCD is considered to be more susceptible to the particle background than the FI because of absence of circuital structures upon a pixel. The increased proton flux seen in the storm period (figure 3) supports this hypothesis.

To evaluate the instrumental non X-ray background (NXB) in the two periods, we utilized the `xisnxbgen` software developed by Tawa et al. (2008). They constructed an NXB database by collecting XIS data when the dark Earth covers the XIS field of view. The NXB spectra (red and blue) of the BI coincide with the TDX spectrum in the pre-storm period (black) above ~ 7 keV, where the NXB dominates the signal. This is a proof of a reliable estimation of the NXB. We supposed that the excess of the TDX spectra against the NXB except for the particle continuum originate from the sky background including diffuse galactic and extragalactic emission and leaked photons from the bright X-ray sources within the field of view.

5. Pre-Storm Period

We wished to investigate the pre-storm period, in order to quantify the sky background and contribution from the bright X-ray sources. For the spectral fitting, we subtracted the NXB from the TDX spectra, and created `rmf` and `arf` files. We used the `xisrmfgen` and `xissimarfgen` programs in the HEASoft package. For the `arf` files, we assumed uniform emission from a region of radius 20 arcmin and corrected obtained X-ray fluxes in spectral fittings for the area of the TDX region. Since we used the χ^2 statistic for our spectral fitting, we binned the spectra to a minimum of 20 counts per bin.

In the spectral fitting model, we took into account two representative diffuse X-ray backgrounds: the local hot bubble (LHB) and the cosmic X-ray background (CXB). We assumed the Raymond-Smith thin-thermal plasma model with $kT \sim 0.1$ keV for LHB based on Snowden et al. (1998). We also used the model Id1 in table 2 of Miyaji et al. (1998) for CXB. In addition, to account for a potential contribution from the bright X-ray sources within the field

of view, we used models in the works of Tamura et al. (1996) and Gaensler et al. (2002). The composite spectrum from the pulsar and PWN can be modelled by an absorbed power law with $N_{\text{H}} \sim 9.5 \times 10^{21} \text{ cm}^{-2}$ and $\Gamma \sim 2.0$. The spectrum of RCW 89 is represented by an absorbed non-equilibrium ionization (NEI) model with $N_{\text{H}} \sim 0.6 \times 10^{21} \text{ cm}^{-2}$ and $kT \sim 0.4 \text{ keV}$. From table 1 of Tamura et al. (1996), we assumed the ionization parameter τ of $6.3 \times 10^{10} \text{ s cm}^{-3}$ and the elemental abundances of 0, 0.18, 0.49, 0.26, 1.12, and 1.1×10^{-2} solar for O, Ne, Mg, Si S, and Fe, respectively. The solar elemental abundance table by Anders & Grevesse (1989) was used. To estimate the contribution from these sources, we let only the normalizations of these four models free.

After fitting tests, we found that the surface brightness of the CXB component is ~ 5 times smaller than the observed continuum. Hence, we fixed all the spectral parameters of CXB as described in Miyaji et al. (1998). We also found that there is a residual around 0.5–0.6 keV, most probably from the neutral oxygen line, and hence added a Gaussian model. Because the spectral fitting was not acceptable at this stage, we finally let the temperature and abundance of Fe in the NEI model free. The obtained result is shown in figure 6 and table 1. Below the errors are 90% confidence range unless otherwise are noted. The model represents the data well with a $\chi^2/\text{d.o.f.}$ of 1.41. It is evident from figure 6 that the soft sky background model dominates the spectrum below 0.7 keV, while the bright X-ray source models reproduce the data above 0.7 keV. The obtained surface brightness of the LHB, $1.7 \times 10^{-15} \text{ erg s}^{-1} \text{ cm}^{-2} \text{ arcmin}^{-2}$, is consistent with the previous observations (Snowden et al. 1998; Hamaguchi et al. 2007; Ezoe et al. 2009). The best-fit temperature of the NEI model also coincides with the temperature of RCW 89 ($0.39 \pm 0.05 \text{ keV}$ in Tamura et al. 1996) within errors, while the iron abundance is an order of magnitude higher.

We estimated that a contribution from the PWN and RCW 89 to the TDX region is ~ 2 and 7 % of their total emission, respectively. Here we cited Gaensler et al. (2002) and Tamura et al. (1996) for the total X-ray fluxes from the PWN and RCW 89, respectively. These numbers are reasonable if we consider the angular response of the Suzaku X-ray telescope (see figure 12 in Serlemitsos et al. 2007). When a point source is located at the center of XIS, 2~3% photons fall outside $r = 6 \text{ arcmin}$. Because the PWN and RCW89 are extended, more photons will fall within the TDX region, which is located $6 \sim 10 \text{ arcmin}$ from the aimpoint. The larger percentage of the thermal NEI component compared to the power-law can be explained by an extra sky background, a so-called transabsorption emission (TAE) (Kuntz & Snowden 2008; Yoshino et al. 2009). The TAE is considered to arise from distant part of the galaxy, above or beyond the bulk absorption of the galactic disk. Its spectrum is described by a thermal emission model with $kT \sim 0.3 \text{ keV}$, comparable to the temperature of RCW 89. Its flux varies depending on the line of direction (Yoshino et al. 2009). The TAE may also explain the Fe line abundance of the NEI component.

6. Storm Period

6.1. Scattering of solar X-rays

Having known that the pre-storm spectrum is dominated by the soft sky background below 1 keV and by the contamination from the bright X-ray sources above 1 keV, we proceeded to study the TDX emission in the storm period. As suggested from figure 5, the major difference between the storm and pre-storm period concentrates below 1 keV. Considering the higher sensitivity of the BI than that of the FI, below we only analyze the XIS BI spectrum. Firstly we investigated the scattering of solar X-rays that was suggested by the X-ray light curve (figure 3) and the spectrum during the pre-storm period (figure 6). In figure 7, the GOES12 solar X-ray fluxes in two energy bands are plotted. The data were taken from the National Geophysical Data Center⁶. An M-class flare occurred at DOY of 235.6 during the pre-storm period. The average X-ray fluxes during the pre-storm period in 1–8 Å or 1.55–12.4 keV and 0.5–3 Å or 4.13–24.8 keV were 3.4×10^{-6} and 4.2×10^{-7} W m⁻², while those during the storm periods were 8.0×10^{-7} and 4.2×10^{-8} W m⁻², respectively. Although the level of the solar X-rays are lower in the storm period, atmospheric expansion associated with the CME can cause an increase of the fluorescence line(s) in the storm period.

With this thought in mind, we changed the data filtering criteria on the ELV angle. The default criteria for the screened data is ELV > 5 deg. In order to investigate a potential difference, we adopted more stringent ELV criteria (ELV > 10, 20, and 30 deg). Figure 8 shows the XIS BI spectra for the four ELV criteria. An increase of a neutral oxygen line at ~0.53 keV is recognized in the ELV > 5 deg spectrum, while there is no significant change between ELV > 10 and > 30 deg in 0.2–5 keV. We obtained the BI spectrum when ELV is 5~10 deg by subtracting the ELV > 10 deg spectrum from that with ELV > 5 deg. Figure 9 is the spectrum after this subtraction. The data is modelled with a single narrow Gaussian model. The parameters are summarized in table 2. The line center energy is consistent with the neutral oxygen K line of 0.524 keV (Thompson et al. 2009)⁷.

By adopting the ELV criteria of > 10 deg, we also noticed that the shape of the light curve also changes. The high count rate events are suppressed. Our result warns that, even if the solar X-ray flux is not high, the standard Suzaku data screening criteria of ELV > 5 deg is not sufficient to remove the scattering component, when the atmospheric density rises after CMEs.

6.2. Solar wind charge exchange

We then analyzed possible enhancements by the exospheric SWCX. To remove the solar X-ray scattering effect, we screened the data with the ELV > 10 deg criteria. In order to

⁶ <http://goes.ngdc.noaa.gov/data/avg/2005/>

⁷ <http://xdb.lbl.gov/>

see differences between the pre-storm and storm periods, we subtracted the pre-storm period spectrum from the storm period. In figure 10 (a), we plot the obtained spectrum. It is evident from figure 10 (a) that the excess clearly contains emission lines between 0.2 and 0.7 keV. The spectrum is built up from a series of emission lines from carbon, nitrogen, and oxygen lines. The spectrum was modelled with seven narrow Gaussians, but the fitting was not statistically acceptable ($\chi^2/\text{d.o.f.}$ of 1.91). In table 3, we list the obtained parameters.

We then tested a theoretical SWCX emission line model developed by Bodewits (2007) (table 8.2), which accounts for the relative emission cross sections for the lines from each of several ions, specifically C V, C VI, N VI, N VII, O VII, and O VIII. In total, 33 lines are involved in this model. Carter, et al. (2010) have successfully fitted the exospheric SWCX spectrum taken with XMM-Newton. We used the tabulated values for a velocity of 600 km s⁻¹, because the average solar wind velocity during the storm period is 530 km s⁻¹. We allowed the six normalizations of the ions to be free. We also added an extra Gaussian to reproduce the lowest energy emission line around 0.25 keV, which is not included in the Bodewits's SWCX model.

In figure 10 (b), we plot the fit results. This SWCX model reproduced the data significantly better than the simple sum of Gaussians with $\chi^2/\text{d.o.f.}$ of 1.46. The obtained parameters are listed in table 4. This acceptable fitting supports the idea that the soft X-ray enhancements during the storm period is due to the exospheric SWCX. The emission line identified around 0.45 keV mainly arises from the $n=4$ to 1 transition of C VI at 459 eV, which is hardly seen in a normal astrophysical plasma and hence is another line of evidence for the exospheric SWCX (Fujimoto et al. 2007).

Figure 11 shows the best-fitting SWCX line energy flux ratio to O VIII compared to the XMM-Newton observation of CME-induced exospheric SWCX by Carter, et al. (2010). While the relative flux ratios from C V to N VII are similar, the absolute values in this Suzaku observation are an order of magnitude higher. Indeed, the O VIII line was prominent in Carter, et al. (2010), while O VII dominates in this observation. We will examine whether this difference can be explained by differences in the incident solar wind O⁷⁺ and O⁸⁺ fluxes and SWCX cross sections in §8.

To investigate a potential influence of the hard continuum originating from the particle background, we fitted the 1–5 keV BI spectrum in the storm period after the subtraction of the pre-storm spectrum with a power-law. The fitting was acceptable with $\chi^2/\text{d.o.f.}$ of 229/190= 1.21. The best-fit photon index and normalization were $0.08_{-0.19}^{+0.17}$ and 26_{-5}^{+6} photon s⁻¹ cm⁻² str⁻¹ (line unit, LU) at 1 keV, respectively. We then extrapolated this power law continuum into the low energy band. We again fitted the BI spectrum shown in figure 10 with a sum of the power law and the SWCX line models. We fixed the photon index and normalization of the power-law component. We then found that all the line normalizations are reduced by 5~20 % but almost all of these parameters are within 90% confidence range listed in table 4. Therefore, the particle continuum may be minor in the low energy band, in comparison with

the SWCX lines.

7. Time Correlation

7.1. *O VII line vs O^{7+} ion*

An X-ray flux of the exospheric SWCX emission can be estimated from an incident solar wind flux and a neutral column density of the exosphere in the line of sight. To assist in this analysis, we utilized the solar wind oxygen ion flux as measured by ACE SWICS⁸. We compared the O^{7+} flux with the XIS BI 0.52–0.6 keV O VII count rate. To eliminate the contribution of the neutral oxygen line, the XIS data are filtered with the criteria of $ELV > 10$ deg. Figure 12 shows the XIS BI 0.52–0.6 keV light curve compared to the SYM-H index, WIND proton flux, and ACE O^{7+} ion flux. As we wrote in §6.1, there is no sign of very high count rate bins due to the scattering of solar X-rays after we filtered the data with the $ELV > 10$ deg criterion. Similar to figure 3, the X-ray enhancement started after the onset of the geomagnetic storm at DOY of 236.25, supporting that the X-ray rise is due to the increased solar wind near Earth and the resultant exospheric SWCX.

Before checking the relation between the X-ray and ion fluxes, we conducted a cross-correlation analysis to know of any time delay between these two data. This procedure requires that both light curves are taken in equally-spaced time intervals. Unfortunately, the ACE ion data has rather low time resolution (2 hr average) and hence we had to bin the XIS BI curve into 8192 s bin. To consider different time bins of these two curves, we interpolated the ACE data to match the XIS curve in the same way as in Ezoe et al. (2010). We then utilized the `crosscorr` software in the HEASoft package with the default mathematical algorithm and normalization method.

In figure 13, we plot the cross correlation. The correlation coefficient has a peak (0.79) at a time delay of 0~8192 s. A null hypothesis probability is 1×10^{-3} , corresponding to $\sim 3\sigma$ significance. The obtained time delay coincides with the expected value of ~ 1 hr. Because the ACE satellite orbits at the L1 point and Suzaku is in the low Earth orbit, about 1 hr time delay is expected between these two data (see §3).

In figure 14, we plot a relation between the O VII count rate and the solar wind O^{7+} ion flux. Because the estimated time delay is consistent with 1 hr, i.e., within the bin size of the light curve, we did not correct the data for the time delay. We can see that two quantities are correlated. We fitted the data with a linear function as shown in a solid line, although the fitting is not acceptable ($\chi^2/\text{d.o.f.}$ of 86.9/14). We checked the relation assuming the time delay of 8192 s, and found a similar increase.

⁸ <http://www.srl.caltech.edu/ACE/ASC/level2/index.html>

7.2. O VII line vs proton

The sparse O⁷⁺ data motivated us to utilize the high time resolution proton data. Using the proton data (100 s average), we checked the time delay and then checked the correlation between the solar wind proton flux and O VII count rate, in the same way as the ion data. Figure 15 shows the cross correlation. A broad peak is seen in the range of 0~3 × 10⁴ sec. This range covers the expected time delay of 1 hr, although the peak is slightly shifted at the positive side (~1.5 × 10⁴ sec), suggesting that there could be an additional positive delay.

Figure 16 displays a correlation between the O VII count rate and the solar wind proton flux. A time delay of 1 hr is assumed based on the satellite positions. The data is represented by a linear function expressed as,

$$C_{\text{XIS}} [\text{cts s}^{-1}] = a \times C_{\text{proton}} [10^5 \text{ cm}^{-2} \text{ s}^{-1}] + b, \quad (1)$$

where a represents the SWCX emissivity and b is an offset emission due to the instrumental and sky background. The fitting was acceptable with $\chi^2/\text{d.o.f.} = 119.5/106$. The best fit a and b are $3.8 \pm 0.7 \times 10^{-7}$ and $2.4 \pm 0.7 \times 10^{-3}$, respectively. The positive b suggests that, even if the solar wind flux is zero, there remains an certain level of background emission. Since the NXB is minor as seen in figure 5, a large part of b must arise from the sky background. We converted b into the photon flux in units of LU based on the O VII fitting in figure 10. Then, b corresponds to 10 ± 3 LU. Yoshino et al. (2009) reported that the O VII line intensity from the soft X-ray background consisting of LHB, TAE and heliospheric SWCX ranges from 2 to 10 LU. Thus, we can interpret b as the sum of these sky backgrounds.

8. Expected Intensity

8.1. Scattering of solar X-rays

The expected oxygen line intensity of the fluorescent scattering of solar X-rays can be estimated from the equation below.

$$P_{\text{scat}} = \frac{1}{4\pi} \int_{E_0} \sigma_{\text{scat}}(E) \eta P_{\text{Sun}}(E) N_{\text{O}+\text{O}_2} dE [\text{LU}], \quad (2)$$

where E_0 is the minimum X-ray energy needed for the fluorescent scattering, $\sigma_{\text{scat}}(E)$ is the photoelectric absorption cross section of oxygen per an atom as a function of X-ray energy E , η is the fluorescent yield, P_{Sun} is the incident X-ray photon flux, and $N_{\text{O}+\text{O}_2}$ is the column density of oxygen atoms and molecules in the line of sight.

We found $\sigma_{\text{scat}}(E)$ from Henke et al. (1993)⁹ and used η of 0.0083 from Krause (1979). We estimated the solar X-ray spectrum based on the GOES data (figure 7) as below. The solar X-ray spectrum is known to be variable and can be expressed by a multi-temperature thin thermal plasma model with the temperature of 0.1~3 keV (e.g., Phillips et al. 1999). For

⁹ http://henke.lbl.gov/optical_constants/

simplicity, we assumed a single temperature plasma and estimated the plasma temperature from the ratio of the two-band GOES X-ray fluxes. We utilized the MEKAL model in the `xspec` software package to simulate the solar X-ray spectrum. The average ratios during the pre-storm and storm periods indicate plasma temperatures of 1.35 keV and 0.98 keV, respectively. We tuned the normalization of the MEKAL model so that the the GOES two-band fluxes are reproduced.

We then multiplied the cross section, fluorescent yield, and solar X-ray spectrum, and then integrated the term as a function of energy from 1 keV, i.e., above the oxygen K-edge (0.54 keV), to 25 keV. We here used 1 keV as a first trial taking into account the lowest energy of the GOES X-ray data (1.55 keV) used to estimate the solar X-ray spectrum. We divided the observed flux by this integral and obtained the necessary $N_{\text{O}+\text{O}_2}$. In the pre-storm period, the observed oxygen line flux was < 2.4 LU (table 1). Then, the necessary $N_{\text{O}+\text{O}_2}$ becomes $< 3 \times 10^{15} \text{ cm}^{-2}$. In the storm period, the line flux was increased by 14 LU (table 2). This corresponds to rise of $N_{\text{O}+\text{O}_2}$ by $4 \times 10^{16} \text{ cm}^{-2}$. Thus, a factor of >10 increase in the column density is suggested. This increase is due to the fact that the solar X-ray intensity was 2 times stronger in the pre-storm period, while the observed neutral oxygen line flux was >5 times weaker compared to that in the storm period.

For comparison, we estimated $N_{\text{O}+\text{O}_2}$ by integrating the atmospheric neutral oxygen atom and molecules of the Sun lit atmosphere in the line of sight, using the NRLMSIS2000 empirical model (Picone et al. 2002)¹⁰. This is an empirical temperature and density model of the Earth's atmosphere from ground to space. We calculated the geodetic latitude, longitude, and altitude of the Suzaku satellite, and integrated the O+O₂ density as a function of time. The density is estimated by a 10 km step from the altitude of Suzaku (~ 570 km during the observation) to 1000 km, and then integrated by multiplying the density at each place by 10 km.

The NRLMSIS2000 model provides us with $N_{\text{O}+\text{O}_2}$ as a function of time. We extracted the average $N_{\text{O}+\text{O}_2}$ in the pre-storm and storm periods. Because the scattering component is seen only in low ELV angles (5 \sim 10 deg), we averaged $N_{\text{O}+\text{O}_2}$ over this ELV range. The estimated $N_{\text{O}+\text{O}_2}$ in the pre-storm and storm periods were $\sim 5 \times 10^{16}$ and $\sim 7 \times 10^{16} \text{ cm}^{-2}$, respectively. This theoretical column density in the storm period coincides with the observation-based value within a factor of 2, while that in the pre-storm period is 20 times larger.

There are two major uncertainties in our estimation. The first one is the assumed lower energy of the solar X-ray spectrum (1 keV). If we integrate the spectrum down to 0.54 keV, $N_{\text{O}+\text{O}_2}$ decreases to $< 0.5 \times 10^{15}$ and $7 \times 10^{15} \text{ cm}^{-2}$ for the pre-storm and storm phases, respectively, owe to the increased solar X-ray photons. If we adopt the lower energy of the GOES data (1.55 keV), $N_{\text{O}+\text{O}_2}$ become $< 3 \times 10^{16}$ and $1 \times 10^{17} \text{ cm}^{-2}$. These numbers can be considered as conservative upper limits. The other is the NRLMSIS2000 model itself. Comparison of the

¹⁰ <http://www.nrl.navy.mil/research/nrl-review/2003/atmospheric-science/picone/>

model with the satellite drag data indicates that there can be a factor of 2 difference (Picone et al. 2002). For example, from the incoherent scatter in the polar upper atmosphere, Ogawa et al. (2009) found that a H density at 600 km altitude is roughly five times higher than the model. Therefore, a factor of 2~5 error can reside in the model. Thus, the observed discrepancy can be reduced by these uncertainties, although the increased $N_{\text{O}+\text{O}_2}$ in the geomagnetic storm, which was not reproduced in the NRLMSIS2000 model, will be left as a future issue.

8.2. Solar wind charge exchange

Next, we estimated the intensity of the exospheric SWCX emission. This is expressed by the equation below.

$$P_{\text{SWCX}} = \frac{1}{4\pi} \alpha P_{\text{SW}} N_{\text{H}} [\text{LU}], \quad (3)$$

where α accounts for the charge exchange cross section and line emission probability, P_{SW} is the incident solar wind flux, and N_{H} is the column density of target hydrogen atoms in the Earth's exosphere.

To calculate N_{H} for the observed O VII line in the storm period, we used α of $6 \times 10^{-15} \text{ cm}^{-2}$ from Wegmann et al. (1998), assuming that all transitions are equally probable. The average ACE O⁷⁺ ion flux of $1.0 \times 10^5 \text{ cm}^{-2} \text{ s}^{-1}$ was used as P_{SWCX} . Then, the observed line flux P_{SWCX} of $\sim 34 \text{ LU}$ provided N_{H} of $7 \times 10^{11} \text{ cm}^{-2}$.

As a consistency check, we estimated an average N_{H} from the O VIII line in the same way. We used α of $4 \times 10^{-15} \text{ cm}^{-2}$ based on Bodewits (2007), the O⁸⁺ flux of $2.0 \times 10^4 \text{ cm}^{-2} \text{ s}^{-1}$, and the observed O VIII flux of $\sim 13 \text{ LU}$. The obtained N_{H} was $2 \times 10^{12} \text{ cm}^{-2}$, a factor of 3 larger than the value estimated for the O VII line. This discrepancy may be explained by uncertainties in the assumed parameters such as the solar wind oxygen ion fluxes measured with ACE and/or α . For instance, if the solar wind velocity in the reaction region is lower (e.g., 200 km s^{-1}) than what we assumed, α for the O VIII line can decrease down to $2.7 \times 10^{-15} \text{ cm}^{-2}$ and N_{H} will increase by a factor of 1.5. Since N_{H} estimated from the O VII line will decrease only by 10% in this case, a part of the discrepancy can be accounted for. If this is the case, the high line flux ratio to the O VIII in this observation (figure 11) may originate from a relatively low O⁸⁺ ion flux compared to that in Carter, et al. (2010).

For comparison, we estimated the neutral density of hydrogen atoms in the Earth's exosphere. We used the Ostgaard et al. (2003) model $n(r)$ for the hydrogen density profile around Earth and limits this to a minimum density of 0.4 cm^{-3} (Fahr 1971). N_{H} can be deduced from the integration of the density in the line of sight as below,

$$N_{\text{H}} = \int_{r_{\text{start}}}^{r_{\text{end}}} n(r) dr, \quad (4)$$

where r_{start} is the distance to the nearest point in the line of sight where the solar wind interacts with the exosphere and r_{end} is the end point of the integration. We roughly assumed r_{start} and r_{end} of 6 and 200 R_{E} , considering the line of sight geometry (figure 1). Here we calculated the

geocentric distance of the point where the geomagnetic field becomes open to space for the first time in the line of sight in the same way as Fujimoto et al. (2007) and defined an average distance during the observation as r_{start} . That is, the region should mainly correspond to the magnetosheath. Then, N_{H} became $2 \times 10^{11} \text{ cm}^{-2}$. Hence, this empirical estimation is ~ 3 and 10 times smaller than the observation-based values for O VII and O VIII, respectively.

One possibility for this inconsistency is the neutral hydrogen density model itself. The hydrogen density may be higher than the model. Another is that more solar wind ions enter into the magnetosphere than we assumed, i.e., $r_{\text{start}} < 6 R_{\text{E}}$. In this case, the SWCX reaction occurs near Earth where the exospheric density is high, leading to a larger theoretical N_{H} .

The latter hypothesis might be supported by other observational facts. Firstly, the X-ray enhancement in figures 3 and 12 coincides with a peak of the geomagnetic storm, corresponding to the duration when many solar wind ions entered into the Earth's inner magnetosphere and caused disturbed ring currents. Secondly, the cross correlation between the high resolution WIND proton data and Suzaku light curve (figure 15) suggests that a positive delay exists even after considering the satellite positions. Thirdly, the exospheric SWCX in the magnetosheath direction found by Ezoe et al. (2010) was an order of magnitude brighter than the model calculation assuming that the SWCX occurs outside the magnetopause. The invasion of the solar wind inside the magnetopause and resultant SWCX reaction can explain the inconsistency as well. Ebihara et al. (2009) suggested that the O^{6+} ions are transported to the inner magnetosphere from the high-latitude magnetopause in August - September 1998 storms driven by CMEs. This result seems to be consistent with the suggestion from the Suzaku observations; the O^{n+} ions may enter into the high-latitude magnetopause through the magnetosheath region. To verify this hypothesis, we need an accurate calculation of solar wind transportation and SWCX reaction and ideally should conduct a direct imaging of the exospheric SWCX at a distant position from Earth in future space missions.

9. Summary and Conclusion

In this paper, we have investigated terrestrial diffuse X-ray emission associated with the strong geomagnetic storm driven by CMEs on 2005 August 23-24 using Suzaku data. This geomagnetic storm was the strongest in terms of the Dst index after the Suzaku launch, as of 2011 April. We found that this event was a textbook case and provided us with a very good opportunity to study the scattering of solar X-rays and the exospheric SWCX. We have obtained following results.

- The X-ray light curve in 0.2–1 keV showed a factor of 2 enhancement, while that in 2–5 keV was almost constant. The enhancement coincided with the geomagnetic storm and increase of solar wind proton and O^{7+} fluxes.
- The X-ray spectrum in the pre-storm period was explained by the sum of diffuse sky

background and leaked photons from bright X-ray sources within the field of view.

- The soft X-ray enhancement in the storm period consisted of two types of terrestrial diffuse X-ray emission. One is the fluorescent scattering of solar X-rays by Earth's low altitude atmosphere seen in low ELV angles ($5 \sim 10$ deg). The other is the exospheric SWCX from highly ionized carbon, nitrogen, and oxygen. After the removal of the scattering component, the X-ray spectrum was well represented by the Bodewits's SWCX model.
- A cross correlation analysis was conducted between the SWCX O VII line and the low time-resolution solar wind O⁷⁺ data. The estimated time delay of < 2 hr was consistent with the expected travelling time of the solar wind (1 hr). The relation between the O VII count rate and solar wind O⁷⁺ flux showed a possible positive correlation.
- The cross correlation between the O VII count rate and the high time resolution solar wind proton flux suggests the existence of an extra delay in addition to the 1 hr delay due to the solar wind travelling time from the satellite position to Earth. The relation between the O VII count rate and the solar wind proton flux was well represented by a linear function. A positive offset in the linear relation suggests that, even if the solar wind flux is zero, there remains a certain amount of X-ray flux due to the sky backgrounds.
- From the observed neutral oxygen line intensity, the column density of oxygen atoms and molecules $N_{\text{O}+\text{O}_2}$ was estimated as $< 2 \times 10^{15}$ and $4 \times 10^{16} \text{ cm}^{-2}$ in the pre-storm and storm periods, respectively. These values are compared with the theoretical NRLMSIS2000 model. $N_{\text{O}+\text{O}_2}$ estimated by the two methods can be consistent with each other considering uncertainties, although a factor of > 20 increase was not consistent with the model and hence will be left as a future issue for the model.
- Similarly, the column density of neutral hydrogen atoms for the exospheric SWCX was estimated as $7 \sim 20 \times 10^{11} \text{ cm}^{-2}$ from the observed O VII and O VIII line fluxes, while the Ostgaard et al. (2003) model predicts $2 \times 10^{11} \text{ cm}^{-2}$. Hence, the calculation may underestimate the neutral column density by a factor of $3 \sim 10$.
- The small column density based on the exospheric density model suggests that our assumption on the SWCX reaction region is not proper and a part of solar wind may enter inside the magnetosphere where the hydrogen density is high.

In conclusion, we have demonstrated that the fluorescent scattering and exospheric SWCX in combination with the solar wind data are quite useful to examine the Earth's atmospheric density models. Following to Ezoe et al. (2010), we conducted the cross correlation analysis and checked the relationship between the X-ray line and solar wind ion flux. This set of analyses must help to study the exospheric density and can provide a global view of the transportation of heavy ion originating from the Sun into geospace, which may contribute to the evolution of a geomagnetic storm.

The authors thank and acknowledge the WIND, ACE, GOES instrument groups for making their data freely available for scientific use. Furthermore, we gratefully acknowledge

the access to Dst and SYM-H indices from the World Data Center for Geomagnetism, Kyoto, Japan.

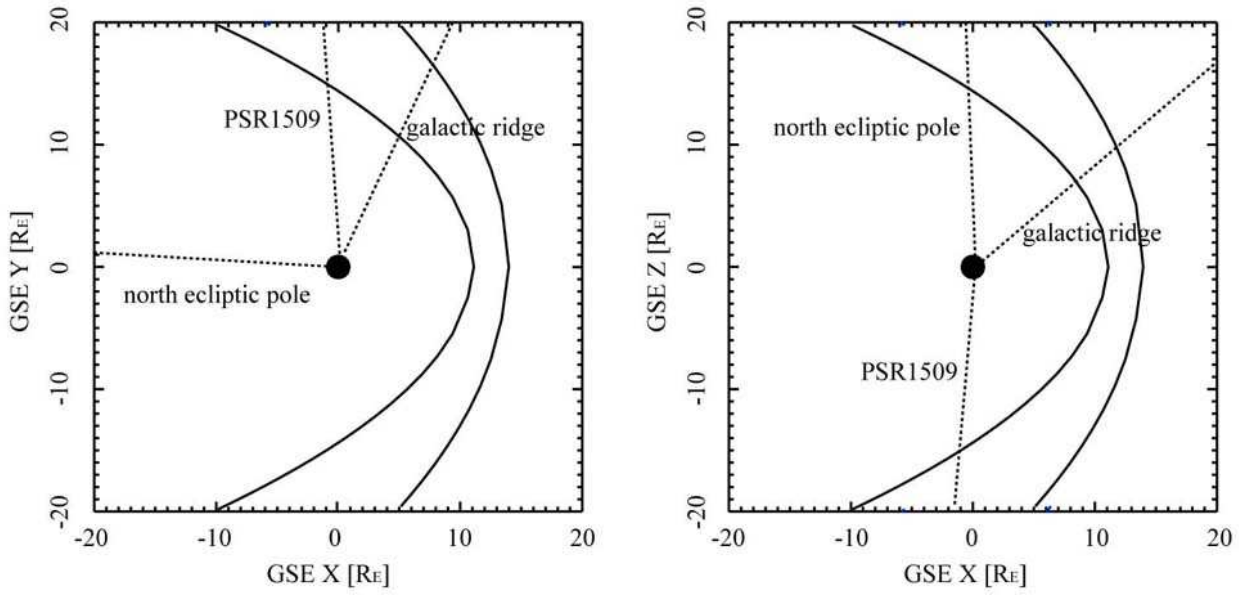


Fig. 1. Line of sight directions in the GSE XY and XZ planes during this observation (PSR 1509), the north ecliptic pole (Fujimoto et al. 2007), and the galactic ridge (Ezoe et al. 2010). Two solid lines indicate approximate positions of the magnetopause and bow shock.

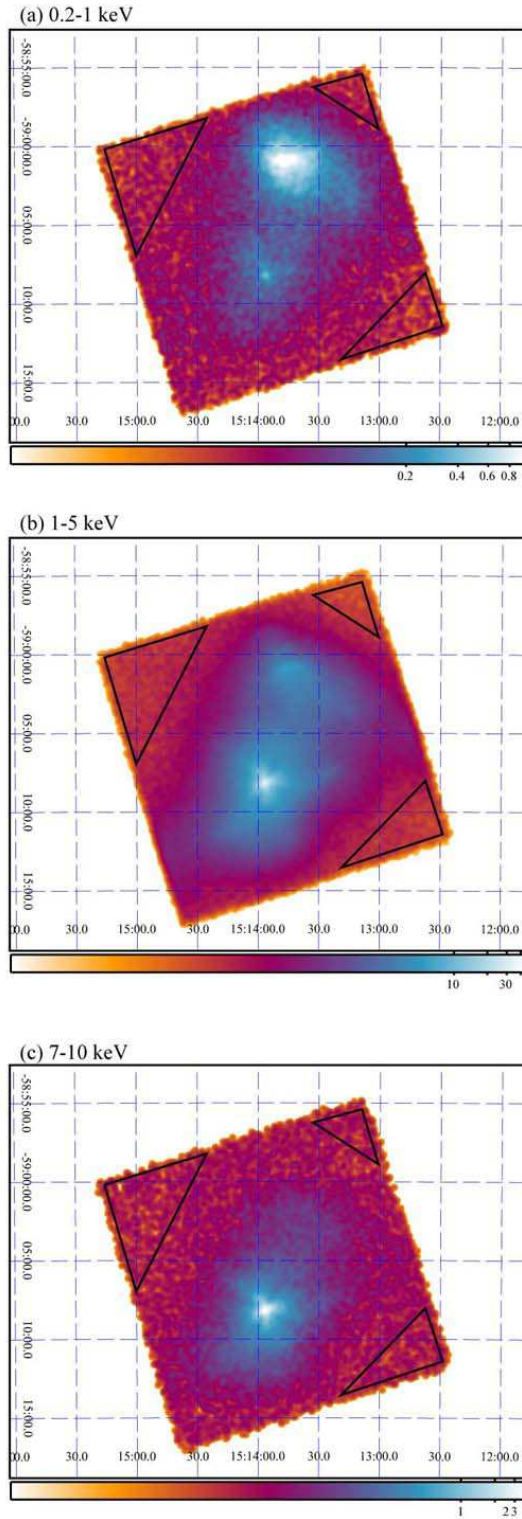


Fig. 2. XIS images in (a) 0.2–1 keV (BI), (b) 1–5 keV (FI), and (c) 7–10 keV (FI). Coordinates are J2000. For clarity, images are smoothed by a Gaussian profile of $\sigma=15$ pixels corresponding to $15''$. The units on the color scales are count per pixel. Solid black lines mark regions utilized in the light curve and spectral analyses.

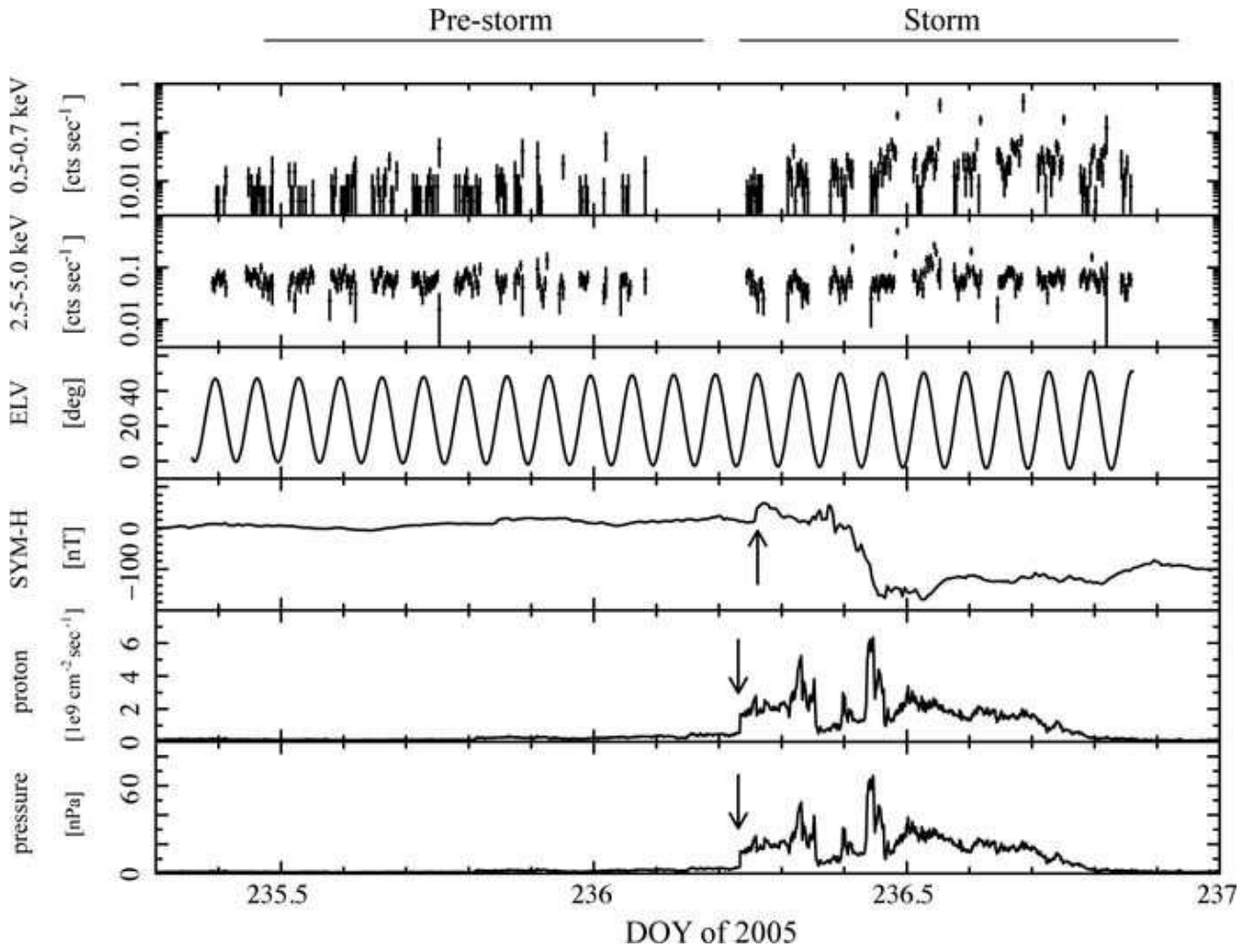


Fig. 3. XIS light curves in 0.5–0.7 keV (BI) and 2.5–5 keV (FI), elevation angle from Earth rim, SYM-H index, solar wind proton flux, and solar wind dynamic pressure as a function of DOY in 2005. The vertical errors are 1σ significance. The proton flux and dynamic pressure were calculated from WIND SWE data (100 s bin). An arrow in the fourth panel shows a signature of the SSC, while those in the fifth and sixth panels indicate increases of the solar wind proton flux and dynamic pressure (see text).

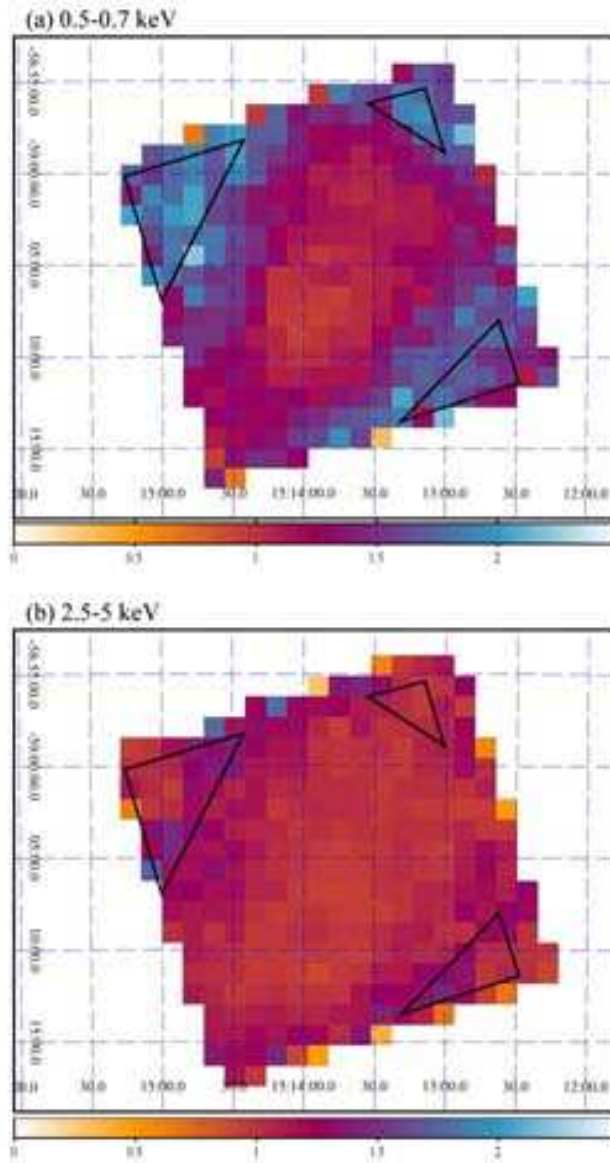


Fig. 4. Ratio maps in (a) 0.5–0.7 keV (BI) and (b) 2.5–5 keV. Each image in the storm period is divided by that in the pre-storm phase. The exposure time difference is corrected. For clarity, images are binned by 64 pixels. The units on the color scales are a ratio. Solid black lines mark the TDX region.

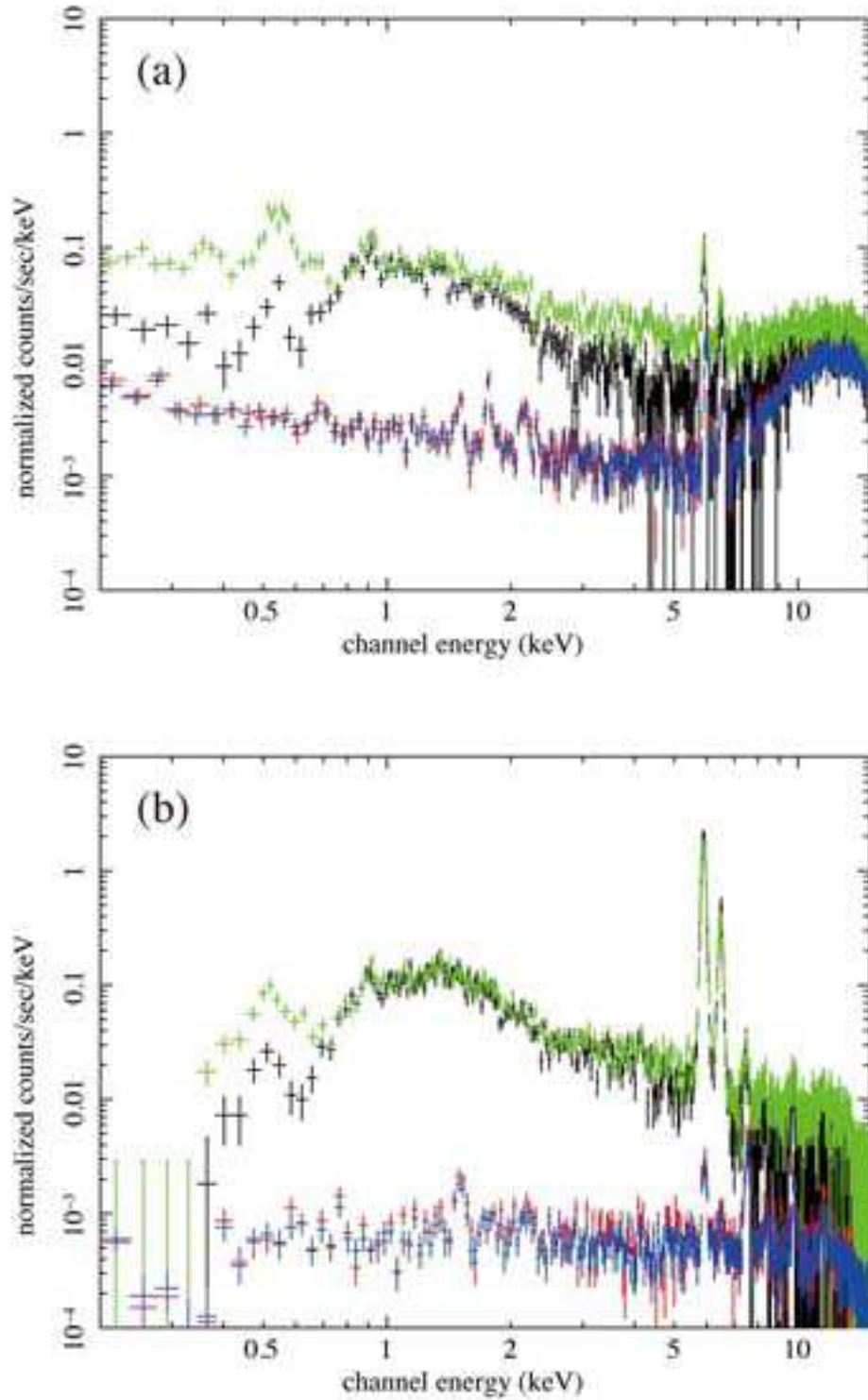


Fig. 5. (a) XIS BI and (b) FI spectra of the TDX region before subtracting backgrounds. Black and green data indicate the spectra during the pre-storm and storm periods. Red and blue data are the NXB estimated for the pre-storm and storm periods. Two distinctive emission lines at 5.9 and 6.4 keV are emitted from a calibration ^{55}Fe sources.

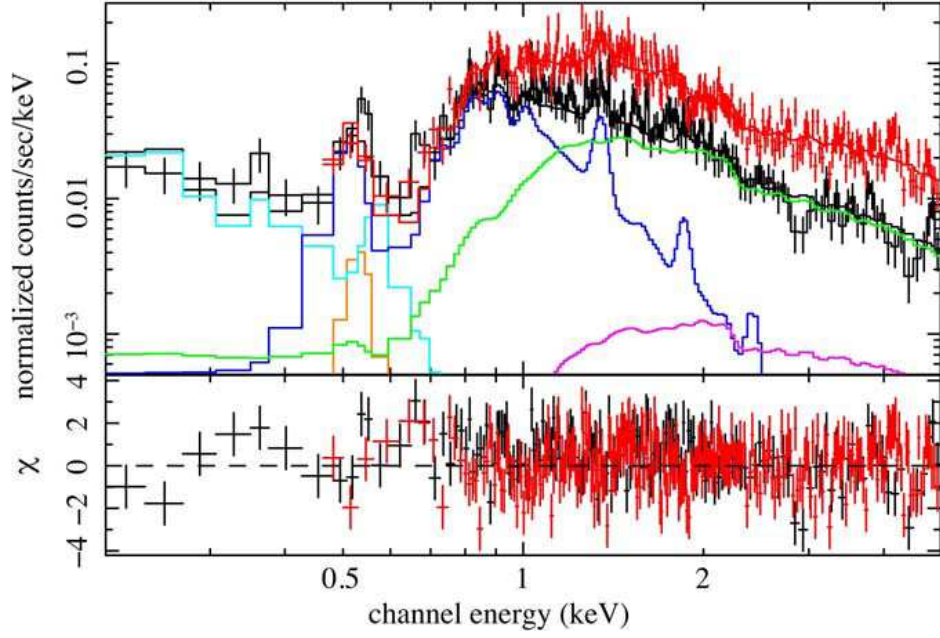


Fig. 6. Background-subtracted XIS BI (black) and FI (red) spectra of the TDX region in the pre-storm period. In the top panel, the solid line is the best-fit model. For clarity, model components are shown only for the BI spectrum and color coded: power law (green), NEI (blue), LHB (cyan), CXB (magenta), and Gaussian (orange). The best-fit parameters are summarized in table 1.

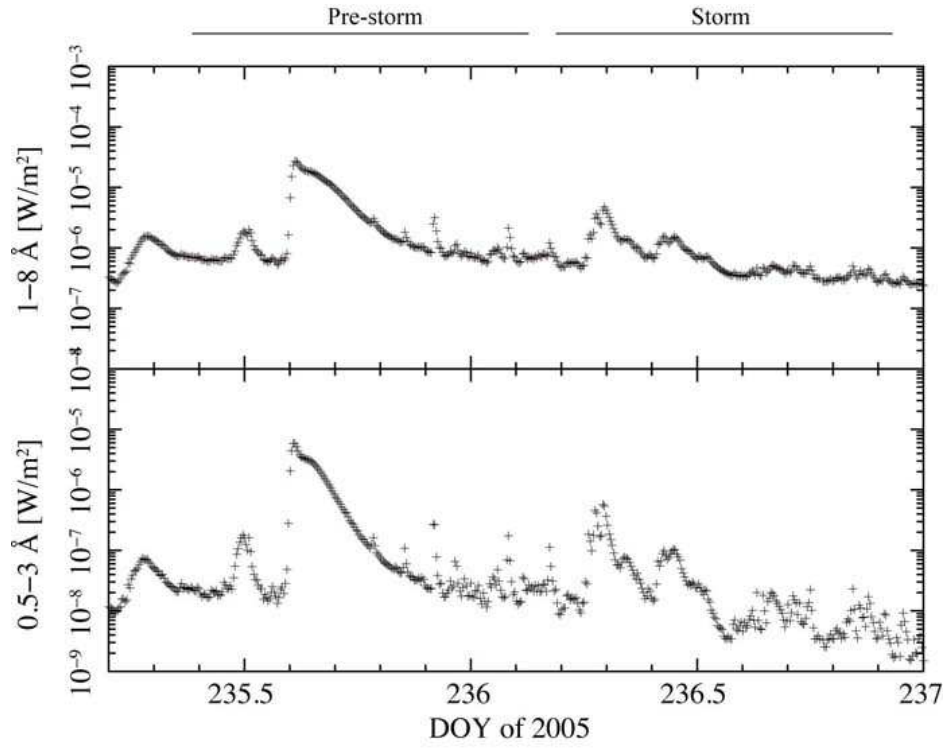


Fig. 7. Solar X-ray fluxes in 1-8 Å and 0.5-3 Å taken with GOES. Two top bars indicate the time range of the pre-storm and storm periods.

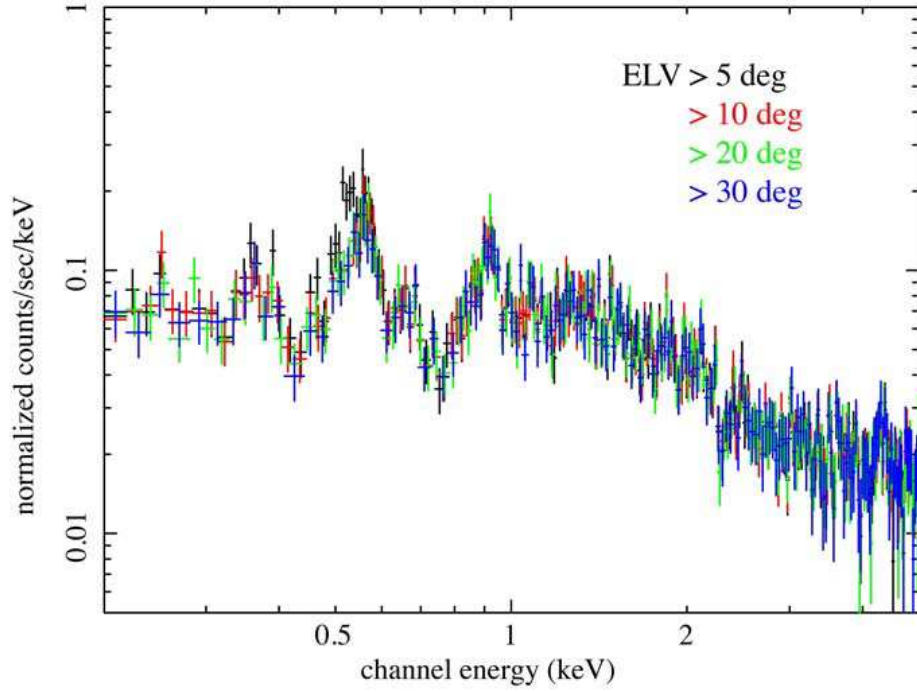


Fig. 8. Background-subtracted BI spectra during the storm period. Different colors correspond to different ELV criteria.

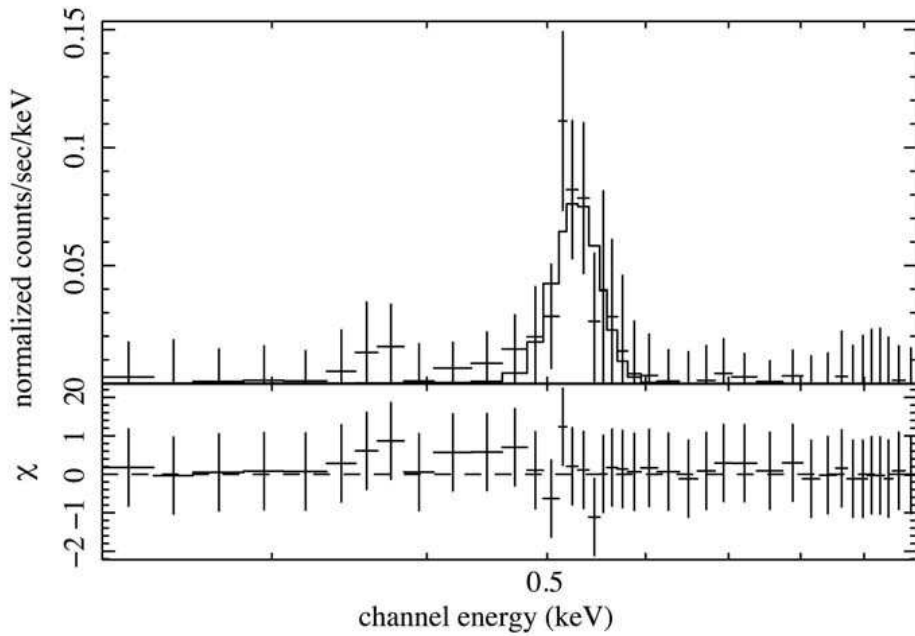


Fig. 9. XIS BI spectrum in the storm period when the ELV angle is 5~10 deg. The solid line in the upper panel is the best-fit Gaussian model. The lower panel shows the data residuals from the model. The parameters are summarized in table 2.

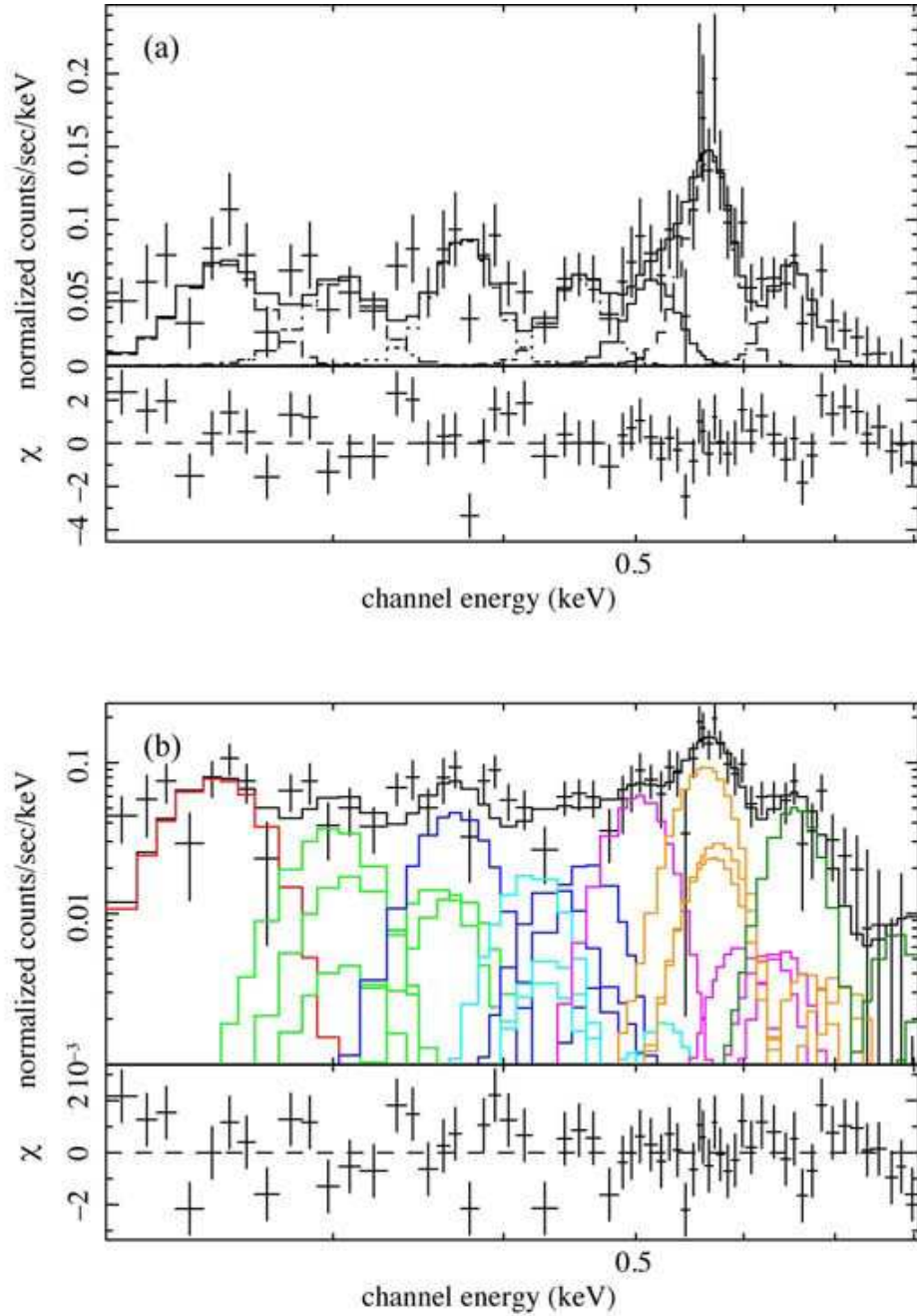


Fig. 10. XIS BI spectrum in the storm period when the ELV angle is > 10 deg. The pre-storm period spectrum is subtracted as a background. In the panel a, the seven Gaussian model is used and the parameters are listed in table 3. In the panel b, the SWCX model is used and the parameters are in table 4. The lines due to C, N, and O are color coded: C V (green), C VI (blue), N VI (cyan), N VII (magenta), O VII (orange), and O VIII (dark green).

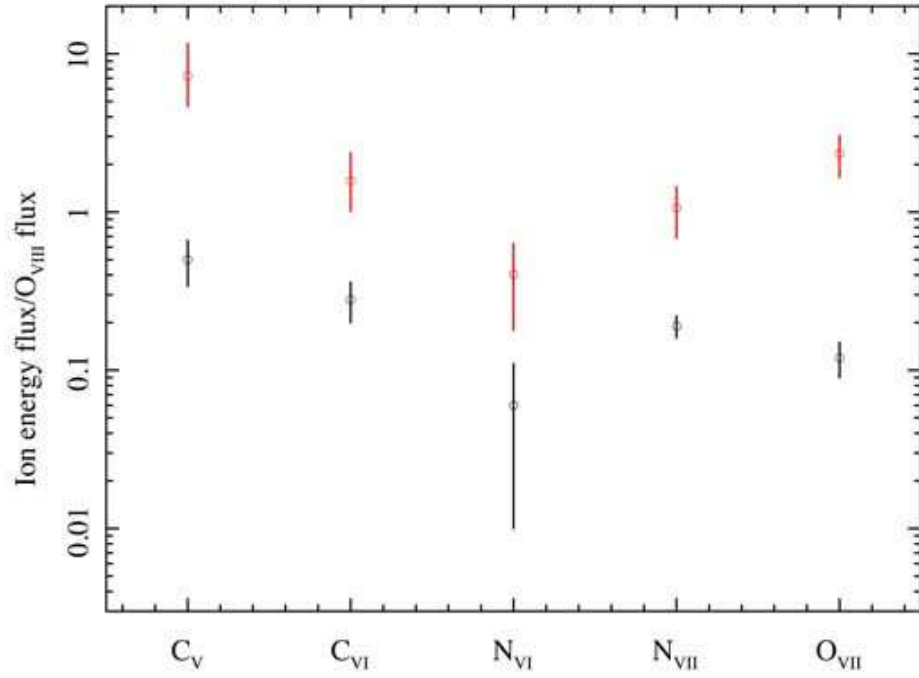


Fig. 11. Line energy flux ratio to O VIII. Red and black data points indicate the best fit parameters of this observation and Carter, et al. (2010), respectively.

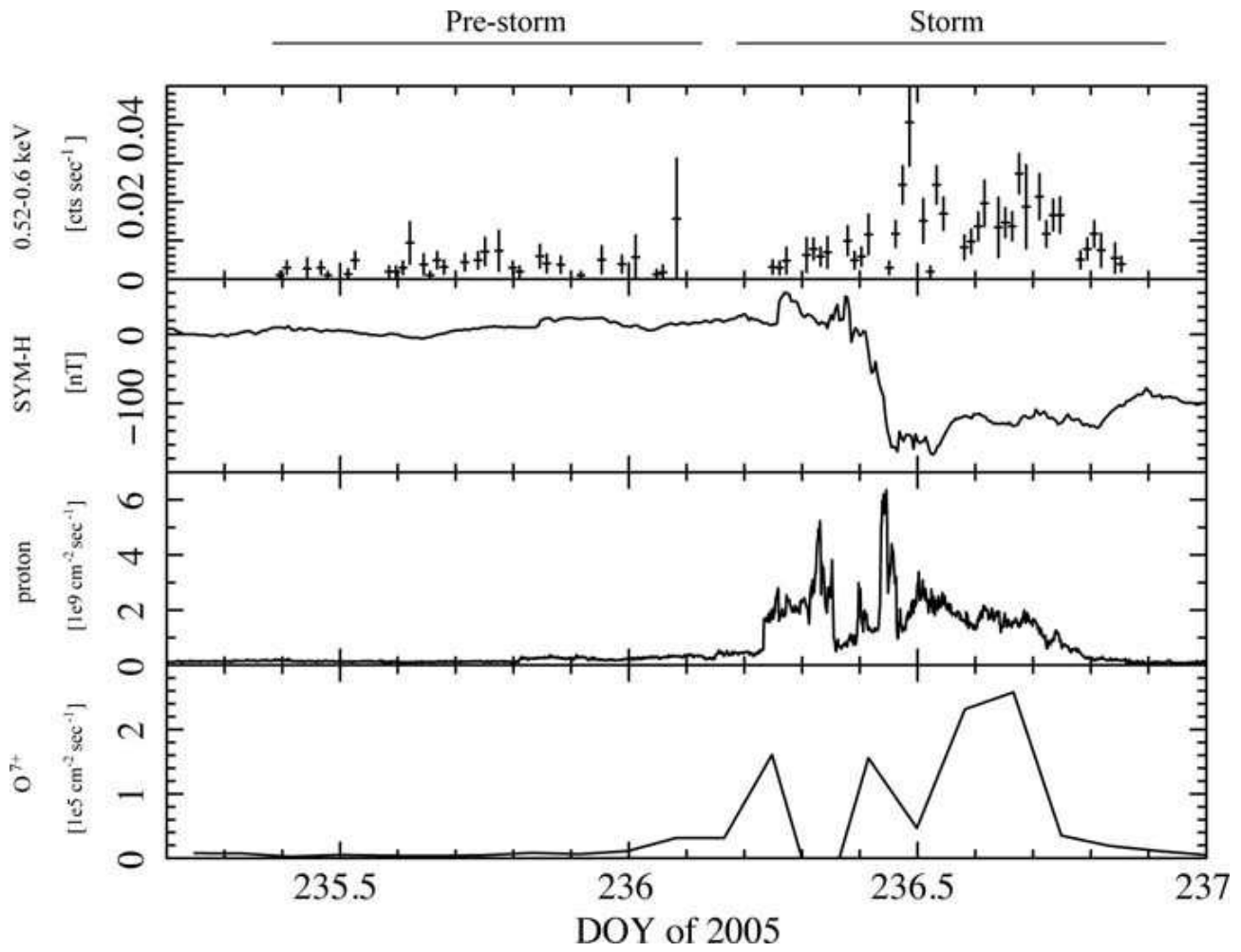


Fig. 12. XIS BI 0.52–0.6 keV light curve filtered with $ELV > 10$ deg, the SYM-H index, the solar wind proton flux, and the solar wind O^{7+} flux from level 2 ACE SWICS data (2 hr bin).

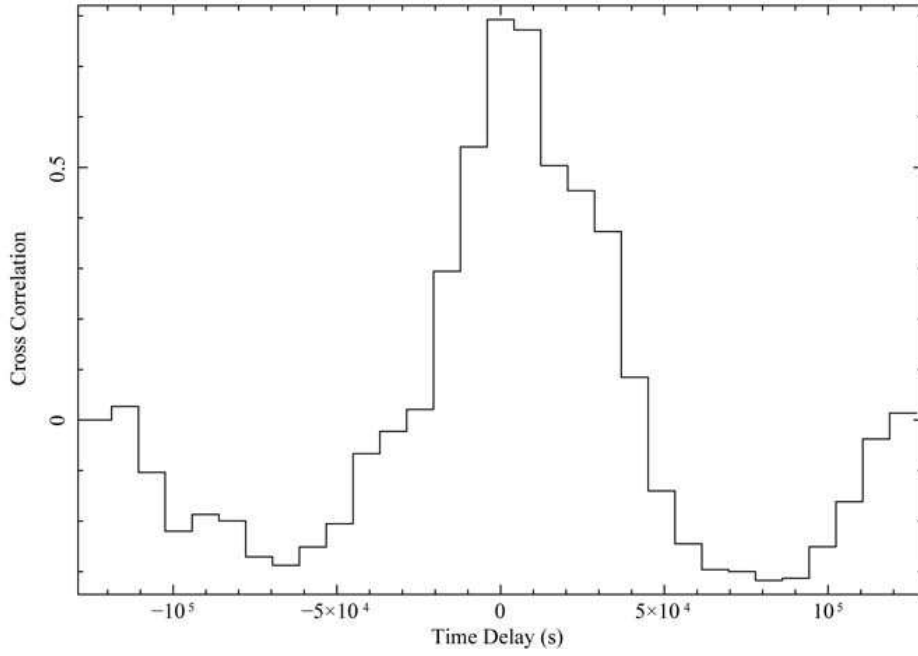


Fig. 13. Cross correlation between the XIS BI O VII count rate and ACE O⁷⁺ flux. A positive delay means that the ACE data leads the XIS BI.

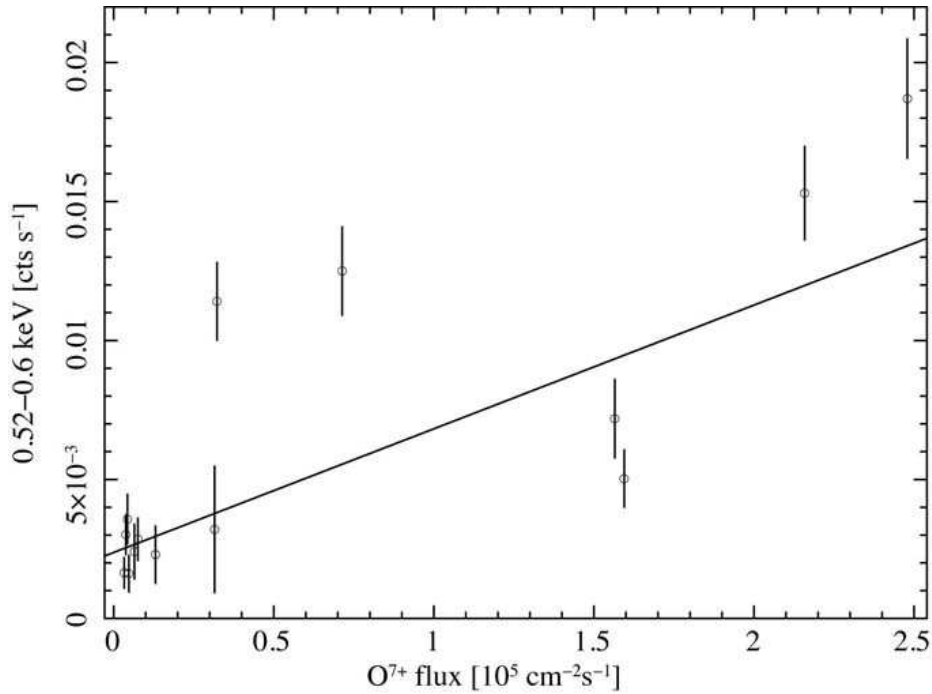


Fig. 14. Correlation between the XIS BI O VII count rate and ACE O⁷⁺ ion flux. The vertical error bar is 1 σ significance. The solid curve is the best-fit linear function.

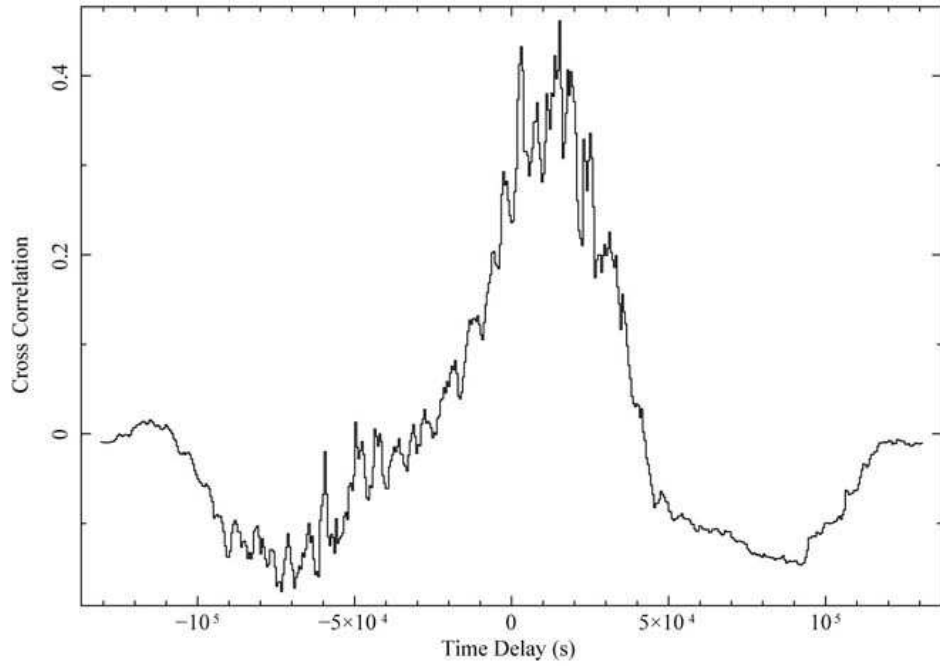


Fig. 15. The same as figure 13 but for the XIS BI O VII count rate and WIND proton flux.

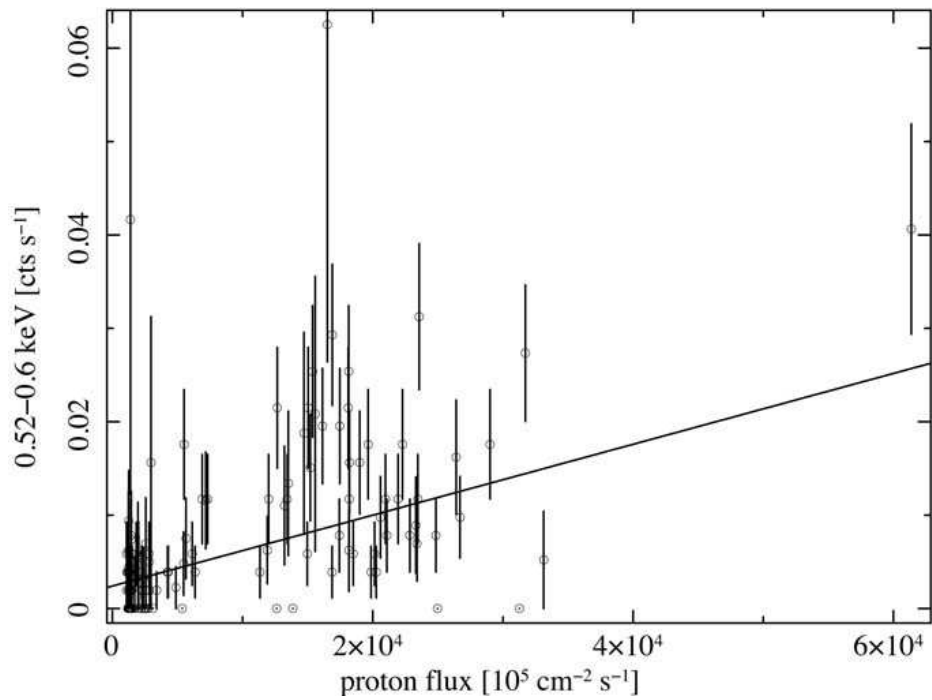


Fig. 16. Correlation between the XIS BI O VII count rate and WIND proton flux. The vertical error bar is 1σ significance. The solid curves are the best-fit linear function.

Table 1. Result of the spectral fit to the pre-storm period shown in figure 6.

Component	N_{H}^{a}	$\Gamma/kT/E_c^{\text{b}}$	Normalization	f_{X}^{c}
Power law ^d	9.5 (fixed)	2.0 (fixed)	$2.2 \pm 0.1 \times 10^2$	1.4×10^{-12}
NEI ^e	0.59 (fixed)	$0.45_{-0.03}^{+0.06}$	$9.6_{-2.1}^{+1.5} \times 10^2$	3.6×10^{-13}
LHB (Raymond-Smith) ^f	0 (fixed)	0.1 (fixed)	15 ± 3	7.1×10^{-14}
CXB (Power-law) ^d	1.4 (fixed)	1.5 (fixed)	10.4 (fixed)	9.4×10^{-14} (fixed)
Gaussian ^g	0 (fixed)	0.53 (fixed)	$0.76 (< 2.4)$	2.2×10^{-15}
$\chi^2/\text{d.o.f.}$	569.3/405			

^a Hydrogen column density in 10^{21} cm^{-2} .

^b Photon index, plasma temperature in keV, or center energy.

^c 0.2–5 keV flux in $\text{erg s}^{-1} \text{ cm}^{-2}$.

^d Normalization is in units of $\text{photon s}^{-1} \text{ cm}^{-2} \text{ str}^{-1} \text{ keV}^{-1}$ at 1 keV.

^e Normalization is in units of $1/4\pi D^{-2} (1+z)^{-2} 10^{-14} \int n_e n_{\text{H}} dV$ per steradians, where D is the angular size distance to the source, and n_e , n_{H} are the electron and hydrogen densities, respectively. The other parameters except for the Fe abundance $Z_{\text{Fe}} = 0.16_{-0.02}^{+0.03}$ are the same as table 1 in Tamura et al. (1996).

^f Normalization is in the same units of the NEI component.

^g Normalization is in units of $\text{photon s}^{-1} \text{ cm}^{-2} \text{ str}^{-1}$.

Table 2. Result of the single narrow Gaussian fit to the spectrum shown in figure 9^a.

E_c	Normalization	f_{X}	Line identification	$\chi^2/\text{d.o.f.}$
$525_{-12}^{+9} \text{ eV}$	14 ± 5	4.2×10^{-14}	O I (524 eV)	6.1/38

^a E_c is the line center energy. Normalization is in units of $\text{photons s}^{-1} \text{ cm}^{-2} \text{ str}^{-1}$. f_{X} is the energy flux in $\text{erg s}^{-1} \text{ cm}^{-2}$. The line width is fixed at 0 eV.

Table 3. Result of the seven Gaussian fit to the spectrum shown in figure 10^a.

Model	E_c	Normalization	f_{X}	Principal line
1	$248 \pm 4 \text{ eV}$	32 ± 8	4.1×10^{-14}	C band lines
2	304_{-5}^{+2} eV	200 ± 50	3.4×10^{-13}	C V (299 eV)
3	$372_{-6}^{+10} \text{ eV}$	40_{-9}^{+6}	8.5×10^{-14}	C VI 2p to 1s (367 eV)
4	$453_{-10}^{+5} \text{ eV}$	13 ± 3	3.5×10^{-14}	C VI 4p to 1s (459 eV)
5	$513_{-12}^{+5} \text{ eV}$	11 ± 4	3.3×10^{-14}	N VII 2p to 1s (500 eV)
6	$565_{-1}^{+10} \text{ eV}$	34 ± 5	1.1×10^{-13}	O VII (f 561 eV, r 575 eV) ^b
7	$650_{-13}^{+7} \text{ eV}$	13 ± 2	4.8×10^{-14}	O VIII 2p to 1s (653 eV)
$\chi^2/\text{d.o.f.}$	89.9/47			

^a Definitions of parameters are the same as in table 2. All the line widths are fixed at 0 eV.

^b f and r denote forbidden and resonance lines.

Table 4. Result of the SWCX model fit to the spectrum shown in figure 10^a.

Ion	Principal energy (eV)	Normalization	f_X
C band lines	244±6 eV	35 ⁺²⁰ ₋₇	4.9×10 ⁻¹⁴
C V	299	200 ⁺¹¹⁰ ₋₅₀	3.4×10 ⁻¹³
C VI	367	32 ⁺¹⁴ ₋₈	7.4×10 ⁻¹⁴
N VI	420	7.7±3.8	1.9×10 ⁻¹⁴
N VII	500	16±4	5.0×10 ⁻¹⁴
O VII	561	36±5	1.1×10 ⁻¹³
O VIII	653	12±3	4.7×10 ⁻¹⁴
χ^2 /d.o.f.	77.6/53		

^a Definitions of parameters are the same as in table 2. Only the principle transitions from C, N, and O plus are listed except for the low energy C band complex. All the line widths are fixed at 0 eV.

References

- Gosling, J.T. 1997, in *Coronal Mass Ejections*, Geophysical Monograph 99, ed Crooker, N.U., Joselyn, J.A., Feynman, J. (American Geophysical Union, Washington) 9.
- Hudson, H.S., Bougeret, J.-L., Burkpile, J. 2010 in *Coronal Mass Ejections*, ed Kunow, H., Crooker, N.U., Linker, J.A., Schwenn, R., Von Steiger, R. (Springer, Dordrecht) 13.
- Gonzalez, W.D., Joselyn, J.A., Kamide, Y., Kroehl, H.W., Rostoker, G., Tsurutani, B.T., & Vasyliunas V.M. 1994, *J. Geophys. Res.*, 99, 5771.
- Miyoshi, Y., & Kataoka, R. 2005, *Geophys. Res. Lett.*, 32, L21105.
- Pilipenko, V., Yagova, N., Romanova, N., & Allen, J. 2006, *Adv. Space Res.*, 37, 1192.
- Petrinec, S.M., McKenzie, D.L., Imhof, W.L., Mabilia, J., Chenette, D. 2000, *J. Atmos. Solar Terr. Phys.*, 62, 875.
- Doornbos, E., Klinkrad, H. 2006, *Adv. in Spa. Res.*, 37, 1229.
- Snowden, S. L., Collier, M. R., & Kuntz, K. D. 2004, *ApJ*, 610, 1182.
- Wargelin, B. J., et al. 2004, *ApJ*, 607, 596.
- Fujimoto, R., et al. 2007, *PASJ*, 59, S133.
- Carter, J.A., & Sembay, S. 2008, *A&A*, 489, 837.
- Ezoe, Y., et al. 2010, *PASJ*, 62, 981.
- Ezoe, Y., et al. 2011, *Adv. Sp. Res.*, 47, 411.
- Carter, J.A., Sembay, S., Read, A.M. 2011, *A&A*, 527, 115.
- Smith, R.K., et al. 2005, *ApJ*, 623, 225.
- Cravens, T.E. 2000, *ApJ*, 532, L153.
- Koutroumpa D., Acero F., Lallement R., Ballet J., Kharchenko V. 2007, *A&A*, 475, 901.
- Koutroumpa D., Lallement R., Kharchenko V., Dalgarno, A. 2009, *Space Sci. Rev.*, 143, 217.
- Carter, J.A., Sembay, S., & Read, A.M. 2010, *MNRAS*, 402, 867.
- Koyama, K., et al. 2007, *PASJ*, 59, S23.
- Mitsuda, K., et al. 2007, *PASJ*, 59, S1.
- Terada, Y., et al. 2008, *PASJ*, 60, S25.
- Gaensler, B. M., et al. 2002, *ApJ*, 569, 878.
- Wanliss, J.A., Showalter, K.M. 2006, *J. Geophys. Res.*, 111, A02202.
- Tawa, N., et al. 2008, *PASJ*, 60, S11.
- Tamura, K., et al. 1996, *PASJ*, 48, L33.
- Hamaguchi, K., et al. 2007, *PASJ*, 59, S151.
- Snowden, S. L., Egger, R., Finkbeiner, D. P., Freyberg, M. J., & Plucinsky, P. P. 1998, *ApJ*, 493, 715.
- Miyaji, T., Ishisaki, Y., Ogasaka, Y., Ueda, Y., Freyberg, M.J., Hasinger, G., & Tanaka, Y. 1998, *A&A*, 334, L13.
- Anders E. & Grevesse N. 1989, *Geochimica et Cosmochimica Acta* 53, 197.
- Serlemittosis, P.J., et al. 2009, *PASJ*, 59, S9.
- Kuntz, K.D., & Snowden, S.L. 2008, *ApJ*, 674, 209.
- Yoshino, T., et al. 2009, *PASJ*, 61, 805.
- Ostgaard, N., et al. 2003, *J. Geophys. Res.*, 108, A7.
- Ezoe, Y., et al. 2009, *PASJ*, 61, S123.

- Thompson, A., et al. 2009, in X-RAY DATA BOOKLET, (Lawrence Berkeley National Laboratory).
- Henke, B. L., Gullikson, G.M., Davis, J.C. 1993, Atomic Data and Nuclear Data Tables, 54, 181.
- Krause, M.O. 1979, J. Phys. Chem. Ref. Data., 8, 307.
- Phillips, K.J.H. et al. 1999, A&A Suppl. Ser., 138, 381.
- Picone, J.M., Hedin, A.E., Drob, D.P., & Aikin, A.C. 2002, J. Geophys. Res., 107, 1468.
- Ogawa, Y., et al. 2009, Geophys. Res. Lett., 36, 24103.
- Wegmann, R., et al. 1998, Planet. Space. Sci., 46, 603.
- Bodewits, D. 2007, Ph D thesis, University of Groningen, The Netherlands.
- Ostgaard, N., et al. 2003, J. Geophys. Res., 108, A7.
- Fahr, H.J. 1971, A&A, 14, 263.
- Ebihara, Y., et al. 2009, J. Geophys. Res., 114, A05219.